# Vibrational Spectroscopic Monitoring of the Gelation Transition in Nafion Ionomer Dispersions

by

Ying Liang<sup>⊥</sup>, Jay P. Kitt<sup>†</sup>, Shelley D. Minteer<sup>†</sup>, Joel M. Harris<sup>†</sup> and Carol Korzeniewski<sup>⊥†</sup>\*

**Abstract.** Infrared and Raman spectroscopy techniques were applied to investigate the drying and aggregation behavior of Nafion ionomer particles dispersed in aqueous solution. Gravimetric measurements aided the identification of gel-phase development within a series of time-resolved spectra that tracked transformations of a dispersion sample during solvent evaporation. A spectral band characteristic of ionomer sidechain end group vibration provided a quantitative probe of the dispersion-to-gel change. For sets of attenuated total reflection Fourier transform infrared (ATR-FTIR) spectra, adherence to Beer's law was attributed to the relatively constant refractive index in the frequency region of hydrated -SO<sub>3</sub> group vibrations as fluorocarbon-rich ionomer regions aggregate in forming the structural framework of membranes and thin films. Although vibrational bands associated with ionomer backbone CF<sub>2</sub> stretching vibrations were affected by distortion characteristic of wavelength-dependent refractive index change within a sample, the onset of band distortion signaled gel formation and coincided with ionomer mass % values just below the critical gelation point for Nafion aqueous dispersions. Similar temporal behavior was observed in confocal Raman microscopy experiments that monitored the formation of a thin ionomer film from an individual dispersion droplet. For the ATR FTIR spectroscopy and confocal Raman microscopy techniques, intensity in the water H-O-H bending vibrational band dropped sharply at the ionomer critical gelation point and displayed a time dependence consistent with changes in water content derived from gravimetric measurements. The reported studies lay groundwork for examining the impact of dispersing solvents and above-ambient temperatures on fluorinated ionomer transformations that influence structural properties of dispersion-cast membranes and thin films.

<sup>&</sup>lt;sup>1</sup> Department of Chemistry and Biochemistry, Texas Tech University, Lubbock, TX 79409-1061

<sup>†</sup> Department of Chemistry, University of Utah, Salt Lake City, UT 84112

<sup>\*</sup> Corresponding author: <a href="mailto:carol.korzeniewski@ttu.edu">carol.korzeniewski@ttu.edu</a>

## 1. Introduction

Solutions containing fluorinated ionomers dispersed in water or water-alcohol mixtures have a long history of application in the preparation of thin films. 1-5 These materials are often used in the formulation of ionically conductive coatings that enhance the selectivity of chemical sensors and bind catalyst particles to bulk current-carrying electrodes in fuel cell and electrolyzer devices. 1,3,6,7 Among fluorinated ionomers, 1,4,8,9 the properties of Nafion have been studied extensively. 1,2,5 Although Nafion thin films and membranes prepared by dispersion-casting at ambient temperatures have limited durability, <sup>1-3</sup> early investigations <sup>10,11</sup> showed materials with structural robustness similar to extrusion-processed commercial membranes result when casting is performed at ca. 140 °C - 160 °C from ionomer dispersed in high boiling point solvents. With the central role of Nafion membranes and ionomer films in electrochemical energy conversion, 1,5,7 in recent years the nanoscale structure of dispersed Nafion particles has been scrutinized as a function of solvent and thermal history and compared to the mechanical properties of cast membranes.<sup>3,12</sup> For Na<sup>+</sup> exchanged ionomers, small angle neutron scattering (SANS) measurements revealed a dependence of ionomer particle dimensions and aggregation behavior on the dispersing fluid chemical nature. In the aprotic solvents studied, processing at 140 °C produced a uniform, reversible gel-phase and high tensile toughness membranes, suggestive of favorable solventionomer interactions facilitating extensive polymer chain entanglement in the cast solid.<sup>3,12</sup> Similar processing in mono- and polyhydric alcohols and aqueous solvent mixtures produced inhomogeneous, thermally irreversible gel-phases and mechanically weaker films. Within each solvent class, a strong correlation was identified between the ionomer critical gelation concentration and the tensile toughness of membranes cast at 140 °C.<sup>3,12</sup>

With interest in recent understanding of ionomer dispersion properties<sup>3,12</sup> and vibrational spectroscopic approaches to ionomer characterization,<sup>9,13,14</sup> we have explored the sensitivity of time-resolved attenuated total reflection (ATR) Fourier transform infrared spectroscopy (FTIR) toward Nafion dispersion transformations during film development. ATR sampling is convenient for recording FTIR spectra of liquids,<sup>15</sup> and thus was simple to adapt for measurements on ionomer dispersions. However, ATR FTIR spectra are sensitive to optical phenomena that can obscure insights into sample properties. Although it is well known that band intensities in ATR FTIR spectra are skewed toward low frequencies because the optical path length within a sample increases in proportion to wavelength,<sup>13,16,17</sup> more difficult to predict and fully compensate are band distortions that result from the interplay of absorption and wavelength dependent back-reflection as infrared radiation propagates the sample-ATR crystal boundary.<sup>13,16,18</sup>

In the reported studies of ionomer dispersions, ATR FTIR spectra are shown to provide quantitative insights when ionomer is present as a dilute analyte within a dispersion and the solvent component dominates the sample refractive index. As solvent becomes a minority component at the sample-ATR crystal interface, spectral changes that can be traced to optical dispersion distortion<sup>13,16,18</sup> develop in bands arising from vibrational modes centered on the structural framework of solid ionomer membranes. Through comparison with gravimetric measurements, the spectral changes are shown to coincide with gel-phase development. A similar sensitivity toward gelation is also demonstrated in confocal Raman microscopy experiments that probe the sample composition within an individual dispersion droplet. The reported measurements, focused on properties of Na<sup>+</sup> exchanged aqueous dispersions<sup>3,12</sup> at ambient temperature, provide a foundation for investigating ionomer dispersion transformations at above ambient temperatures and in non-aqueous solvents carefully selected to minimize spectral interferences.

## 2. Experimental Section

- 2.1 Reagents. Aqueous, Na<sup>+</sup> exchanged (~5 wt %) Nafion dispersion was prepared from stock Nafion dispersion (1100 g/eq, 10 wt % in water (Sigma-Aldrich, St. Louis, MO USA)). Approximately 1.0 mL of the stock dispersion was pipetted into the tubing of a dialysis device (Spectra-Por Float-A-Lyzer G-2, 3.5-5 kD molecular weight cutoff (Spectrum Labs, Saint Paul, MN USA)) and cation-exchanged for 12 h against 0.1 M NaOH (prior to addition of sample, the dialysis tubing was cleaned by thorough rinsing in deionized water and 0.1 M NaOH solution). Subsequently, the device was placed in deionized water (8 h with a change in rinse water every 2 h) to remove excess NaOH. Afterward, the aqueous dispersion was transferred with a pipet to a clean glass vial for storage. The ionomer mass percent and dispersion density were determined from the mass of a 150 μL aliquot measured to  $\pm$  0.1 mg before and after evaporation of the solvent.<sup>3,12</sup> All other chemicals were reagent grade or better and used as received.
- 2.2 Instrumentation. FTIR spectra were collected using a Bruker Vertex-70 spectrometer. Single beam spectra were collected at 4 cm<sup>-1</sup> resolution, with 128 scans averaged, and processed using OPUS version 7.0 (Bruker) software. The instrument bench and sample compartment were continuously purged with dry air from a purge gas generator (Parker-Balston Model 75-52, Parker-Hannifin Corp.). ATR FTIR spectra were collected with the use of a VeeMAX II accessory (Pike Technologies, Madison WI USA) equipped with a single reflection, 45° ZnSe ATR crystal containing a circular, 20-mm diameter sampling surface (Pike Technologies). A liquid cell constructed from poly(tetrafluoroethylene), PTFE, mounted to the ATR crystal assembly to facilitate measurements on ionomer dispersion samples. The starting dispersion volume was adjusted to produce a condensed film thickness of ~20 μm to ensure the sample thickness remained greater than the evanescent wave penetration depth at the lowest frequency of interest (950 cm<sup>-1</sup>).

Results of electromagnetic field calculations that examine radiation propagation through the ZnSe/Nafion film boundary and effects of film thickness on spectral features are included in the Supplemental Material (Section 1 and Figures S1-S3). Measured ATR FTIR spectra are displayed in units of pATR, where pATR =  $-\log (I_{sample} / I_{reference})$ , and  $I_{sample}$  and  $I_{reference}$  represent the sample and reference single-beam spectra, respectively.

The confocal Raman microscope system has been described in detail. <sup>19</sup> The excitation source was a single-longitudinal-mode diode laser operating at 638 nm. The beam was spatially and spectrally filtered and then expanded to fill the rear aperture of a 100 ×, 1.4 N.A. oil immersion objective (Nikon, Plan APO VC) mounted on an inverted fluorescence microscope frame (Nikon Eclipse TE-200). <sup>19</sup> Samples were analyzed as individual droplets. An aliquot of aqueous dispersion (40  $\mu$ L) was dispensed onto a glass microscope coverslip (No. 1.5 thickness, BK-7 glass) positioned on the microscope stage. The droplet was covered by a small glass vessel (~10 mL), that provided space to accommodate solvent evaporation, while shielding the droplet from laboratory air currents. The expanded diode-laser beam radiation was directed through the microscope objective, immersion oil and coverslip and was brought to a focus within the aqueous droplet about 5  $\mu$ m above (z-dimension) the coverslip-aqueous dispersion boundary. Sampling at  $z \approx 5 \mu$ m ensured the confocal probe volume<sup>20,21</sup> (~5 fL at 90 % detection efficiency)<sup>19</sup> was fully localized within the sample. Reported spectra represent the average of 20 acquisitions each collected with a 30-s integration time.

Gravimetric measurements were performed with the use of a high sensitivity (0.01 mg) analytical balance (Mettler-Toledo, (Columbus, OH) Model XS205DU). The gravimetric water loss simulation was carried out on a desktop computer using a spreadsheet (Microsoft Excel) program.

All spectroscopic and gravimetric measurements were performed at the constant temperature  $21.0 \pm 0.5 \, \text{C}^{\circ}$  and relative humidity (< 30 %) in an ambient laboratory atmosphere.

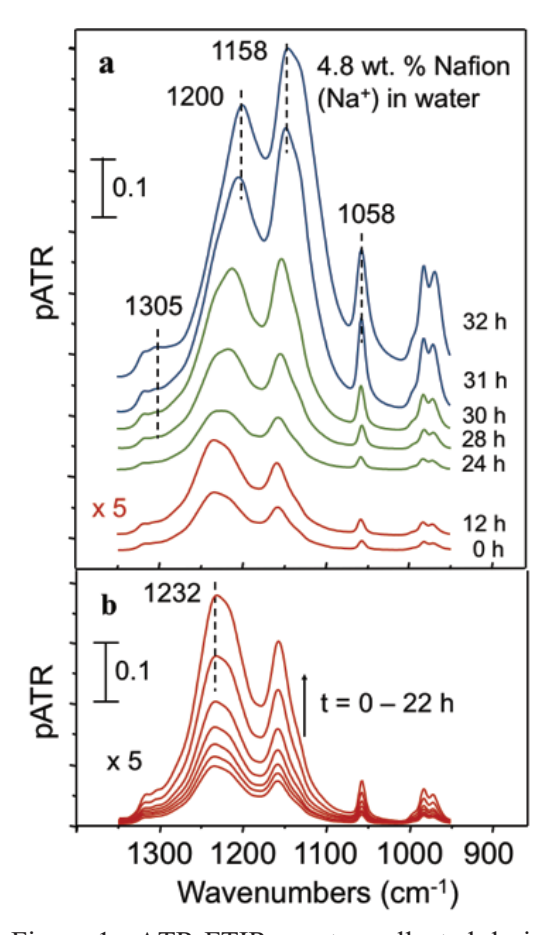
2.5 Ionomer dispersion density estimation. Ionomer dispersion densities ( $d_{dispersion}$ ) were calculated by treating the dilute dispersion as an ideal solution, allowing the solution volume ( $V_{solution}$ ) to be determined from the sum of individual ionomer and water contributions. The latter were estimated from the density of bulk Nafion (1.9 g/mL)<sup>22</sup> and water (1.0 g/mL) at 25 °C. Specifically,  $d_{dispersion}$  values were calculated from the mass of ionomer ( $m_{ionomer}$ ) and water ( $m_{water}$ ) components as follows:

$$d_{dispersion} = \frac{(m_{ionomer} + m_{water})}{V_{solution}},$$

where  $V_{solution} = [m_{ionomer} \times \left(\frac{1}{1.9} \frac{mL}{g}\right) + m_{water} \times \left(\frac{1}{1.0} \frac{mL}{g}\right)]$ . The approximation predicted  $d_{dispersion}$  to within 2 %, when applied to Nafion dispersions  $\leq 15$  wt %, which is the point when the sample viscosity becomes too great for accurate volume measurement. The estimated values of  $d_{dispersion}$  were used to convert between molarity and wt % in expressing ionomer dispersion content.

### 3. Results and Discussion

3.1. ATR FTIR measurements. Figure 1 shows ATR spectra that follow changes in ionomer features during the transformation of an aqueous dispersion to a thin film. The 1400 cm<sup>-1</sup> - 800 cm<sup>-1</sup> range displayed contains the major infrared bands of the ionomer and is free of solvent interferences, since water vibrations are outside the range plotted.<sup>23-28</sup> The assignment of Nafion infrared bands has been of longstanding interest (c.f., Refs. 24,25,29-33). The strong peaks near 1230 cm<sup>-1</sup> and 1150 cm<sup>-1</sup>, reflective of features in PTFE,<sup>25,34</sup> contain the ionomer backbone C-F stretching vibrations and are broadened by overlap with modes centered on functional groups in



<u>Figure 1</u>. ATR FTIR spectra collected during the development of a Nafion thin film from an aqueous 4.8 wt % dispersion of the ionomer (1100 EW, Na<sup>+</sup> exchanged form). Spectral series spanning (a) the full measurement time range and (b) period associated with the dispersion. The color scheme indicates the dispersion (red), gel (green) and solid membrane (blue) phases.

the sidechains.<sup>24-27,32,33</sup> The lower energy bands near 1058 cm<sup>-1</sup> and in the 980-950 cm<sup>-1</sup> region are associated with vibrations of sidechain functional groups.<sup>25,30-33,35</sup> Density functional theory (DFT) calculations have shown the normal modes are composed of strongly coupled -SO<sub>3</sub><sup>-</sup> and C-O-C motions.<sup>32,33,35</sup>

Typically, infrared spectroscopic studies of Nafion have interrogated fully formed membranes and thin films with focus on elucidating ionomer structure or properties of imbibed solvent. 13,26-28,33,36-38 Investigations of the dilute ionomer dispersions that are the precursors to cast ionomer materials are considerably less common, deterred by solvent interferences that have potential to overwhelm ionomer vibrational signals and by complications of handling a liquid sample. In

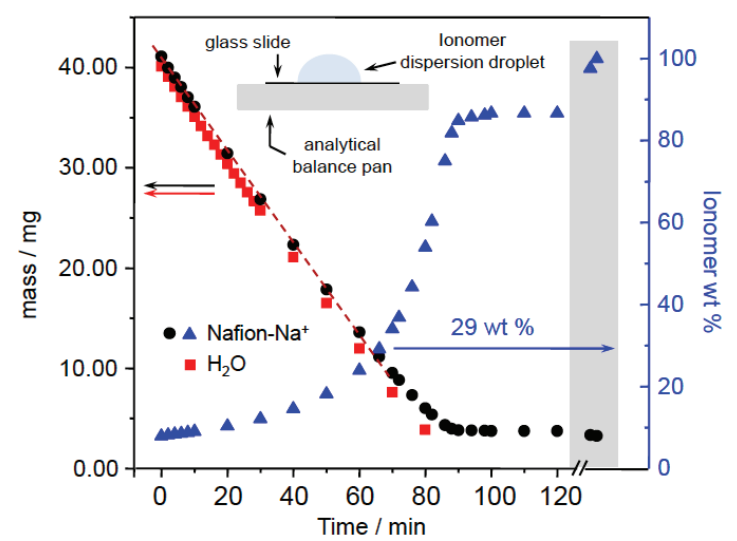
recording the spectra in Figure 1, the advantages of the ATR FTIR technique (i.e., simplicity in liquid handling and ability to optimize the pathlength for measurements on aqueous solutions<sup>15,39</sup>) made it possible to detect vibrations of the ionomer dispersed down to a few wt % in water.

The spectra collected over the first 22 hours, shown on an expanded scale in Figure 1b, have characteristics of a dilute analyte. The band intensities grow as the ionomer concentration increases, while the shapes and peak positions remain unchanged, indicating the ionomer remains

well solvated and unperturbed by ionomer-ionomer (e.g., analyte-analyte) interactions during this early period of evaporative solvent loss. As discussed further below, this dilute analyte behavior enables the spectral data to be applied to estimate ionomer concentration in the dispersion, and subsequently, to identify the dispersion-to-gel transition region. At longer times (> 22 h), the spectra in Figure 1 begin to develop strong band shape changes at frequencies of the ionomer backbone vibrations (1300 cm<sup>-1</sup> - 1100 cm<sup>-1</sup>). The spectral variations track with gel-phase formation, but as elaborated in Section 3.3, have complicated origins.

3.2. Gravimetric measurements. To assist in the quantitative analysis of the time-resolved ATR FTIR spectra collected, gravimetric measurements were performed to gain insights into the expected concentration dependence of ionomer during film formation from the dispersion. The plot in Figure 2 shows changes in the mass of a Nafion aqueous ionomer dispersion droplet

deposited onto a glass (SiO<sub>2</sub>) microscope coverslip during solvent evaporation into quiescent ambient atmosphere. The response for a pure water droplet is included. The steady decline in the traces at early times (< ~60 min) is typical for evaporation of water-rich droplets that maintain a constant area of contact with the substrate. <sup>40,41</sup> The trend is similar for pure water and the dispersion during this period, although the rate of water



<u>Figure 2</u>. Plot of mass versus time for a 40  $\mu$ L droplet of (black circles) Nafion ionomer (1100 EW, Na<sup>+</sup> exchanged form) dispersion in water at 7.4 wt % and (red squares) deionized water, dispensed onto a glass slide on the platform of a high sensitivity analytical balance. The blue triangles trace the mass change of the ionomer droplet expressed as mass %. The dashed line is the least squares fit to the black symbols covering the 0-60 min period (R<sup>2</sup> = 0.999). The points in the shaded region indicate the mass after overnight drying followed by 30 min of oven drying at 120 °C.

loss from the dispersion is slightly slower. The slower loss rate relative to the pure solvent likely can be explained by attractive water-Na<sup>+</sup> interactions in the dispersion, as the water evaporation rate from the dispersion tracked closely with the response for an aqueous droplet containing an equivalent initial Na<sup>+</sup> concentration (0.05 M NaCl).

At longer times (> 60 min), the rate of mass change in the dispersion droplet becomes nonlinear. The behavior reflects effects of ionomer densification, such as trapping of condensed water within the polymer matrix and chemical composition changes at the substrate-droplet-air boundary where the evaporation rate is expected to be fastest. Figure 2 also includes the time-dependent changes for the ionomer droplet expressed in terms of ionomer mass percent, where

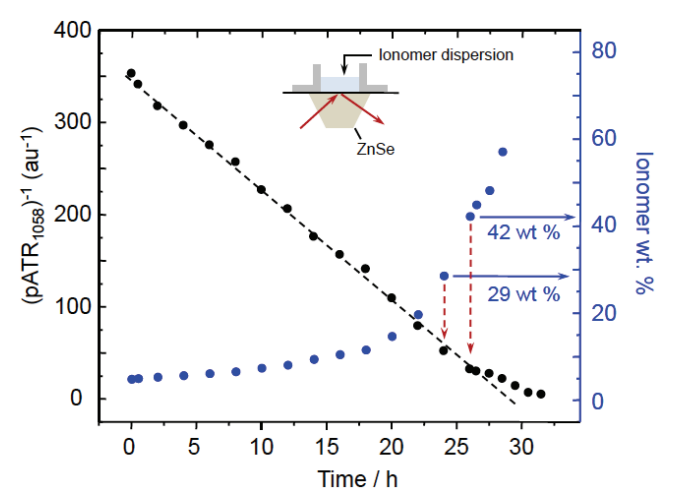
ionomer 
$$wt \% = \left[\frac{m_{ionomer}}{(m_{ionomer} + m_{water})}\right] \times 100\%.$$
 (1)

Since the ionomer mass remains constant during the solvent evaporation period, the ionomer mass % trends inversely with changes in droplet water content.

The dashed line in Figure 2 highlights the constant rate of mass change in the dispersion droplet at early times. Extrapolating the line, and mapping to the ionomer wt % scale, shows the rate slows as the ionomer composition approaches 29 wt %, just ahead of the critical gelation point ( $\sim$ 34  $\pm$  4 wt %)<sup>3</sup> for the aqueous ionomer dispersion. Although the time dependence of the mass change in the dispersion droplet can be influenced by several factors (i.e., ionomer and mobile cation hydration and composition gradients that drive fluid flow),<sup>41-46</sup> the results in Figure 2 indicate the dilute dispersion behavior and characteristic rate of water escape persists until the droplet enters the gel-phase transition region. Notably, a similar sensitivity to gel-phase formation, in this case through assessment of droplet volume change, has been observed for evaporating droplets of a dilute silica nanoparticle dispersion.<sup>43</sup> The least squares fit line to the water droplet data in Figure 2 was omitted for clarity. However, the data over the full measurement range fit a linear model

with coefficient of determination,  $R^2 = 0.999$ , confirming the expected pure solvent response was obtained.

3.3. Quantitative analysis of ATR FTIR spectra. Similar to the gravimetric data in Figure 2, the time series of ATR FTIR spectra in Figure 1a contain evidence of the ionomer dispersion-to-gel transition region. Across the time series, the spectral band intensities steadily increase, even beyond the 22 h point. During this latter period, the characteristic PTFE features between 1230 cm<sup>-1</sup> - 1160 cm<sup>-1</sup> linked to vibrations on the fluorocarbon-rich thin film framework undergo changes in shape and position, while bands centered on vibrations of functional groups in the ionomer sidechains (i.e., 1058 cm<sup>-1</sup> and 980-950 cm<sup>-1</sup>) show considerably less position and shape variation. Composed of hydrophilic groups (i.e., -SO<sub>3</sub>-, C-O-C), the sidechains retain water to a greater extent than the TFE backbone as the dilute dispersion transitions to the thin film form and its characteristic nanoscale phase-separated ion conducting pore and channel structure.<sup>1,2,5,47</sup> The



<u>Figure 3</u>. Data derived from the full ATR FTIR spectral dataset. Black symbols, left y-axis: The inverse of pATR<sub>1058</sub> plotted versus time. Blue symbols, right y-axis: Ionomer mass % derived from pATR<sub>1058</sub> (see text for details). The dashed line is the least squares fit to the data covering the 0-24 h period ( $R^2 = 0.997$ ). The inset sketch depicts the ATR FTIR sampling configuration adapted for the measurements.

water-rich environment surrounding the sidechains helps maintain a nearly constant refractive index in the frequency regions of the -SO<sub>3</sub><sup>-</sup> and C-O-C group vibrations, thereby limiting optical distortion in these bands during film formation. As a consequence, with properties of a well-solvated analyte the 1058 cm<sup>-1</sup> feature, arising from coupled vibration of sidechain terminal -SO<sub>3</sub><sup>-</sup> and C-O-C groups, <sup>32,33,35</sup> provides an

excellent marker for quantitation of ionomer dispersion concentration change during film development.

Building on this latter advantage, the band intensity at 1058 cm<sup>-1</sup> (pATR<sub>1058</sub>) can be correlated to the ionomer molar concentration (C) using Beer's law: pATR =  $\varepsilon d_{eff} C$ , where  $\varepsilon$  is the molar extinction coefficient and  $d_{eff}$  is the effective light penetration depth, or pathlength into the sample. If C is expressed as the ratio of ionomer moles to  $V_{solution}$ , the Beer's law relationship can be rearranged to give:

$$pATR^{-1} = k' + k''V_{solvent}, (2)$$

where  $V_{solvent}$  is the solvent (water in this case) volume and k' and k'' are constants, with k' proportional to the ionomer volume ( $V_{ionomer}$ ) contribution. (Note:  $V_{solution} = V_{solvent} + V_{ionomer}$ .)

When the rate of solvent loss (a) is fixed, the change in solvent volume with time, t, can be written in terms of the initial solvent volume ( $V_{solvent}^o$ ) as  $V_{solvent} = V_{solvent}^o - at$ . Substituting into Eq 2 gives:

$$pATR^{-1} = k' + k'' V_{solvent}^o - k''a t.$$
(3)

Eq 3 shows a plot of pATR<sup>-1</sup> versus time is expected to decrease linearly with a slope proportional to the solvent evaporation rate.

The black symbols in Figure 3 plot (pATR<sub>1058</sub>)<sup>-1</sup> with time for the data in Figure 1. The roughly linear response between the start of data collection up to the 24 h point reflects the loss of solvent according to Eqs 2 and 3. The trend is similar to the ionomer droplet mass changes displayed in Figure 2, with the longer ATR FTIR data collection period ascribed to the different experimental platforms and solution volume requirements. Beyond the initial 24 hour period, (pATR<sub>1058</sub>)<sup>-1</sup>

begins to change more slowly. Mapping the response to the wt % scale (Figure 3, blue symbols) shows the  $\sim 34.2 \pm 3.9$  wt % critical gelation point<sup>3</sup> is encompassed within the 24 h - 26 h range.

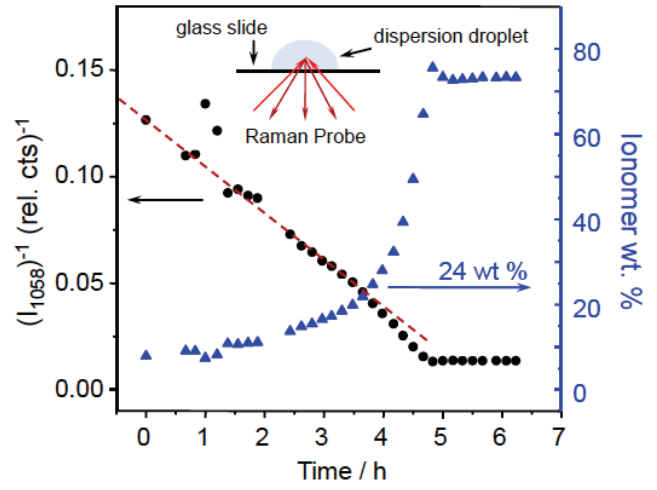
In Figure 3, as a first step to determining the ionomer wt % values displayed (blue symbols), ionomer molar concentration was estimated from pATR<sub>1058</sub> using Beer's law. The initial (t = 0) sample molarity derived from the ionomer equivalent weight (1100 g/eq) and the measured sample mass percent (4.8 wt %) and density (1.02 g/mL) was used as a calibration point. Since the ionomer mass remains constant throughout an experiment, changes in pATR<sub>1058</sub> correlate directly to changes in  $V_{solution}$ , enabling estimation of  $d_{dispersion}$  and ionomer wt % at each time point.

Inspecting Figure 1 further, at the 24 h point a low frequency shoulder becomes evident on the 1232 cm<sup>-1</sup> and 1158 cm<sup>-1</sup> bands, and at longer times, the relative intensity of the two peaks undergoes marked changes. Given the bands trace to signature ionomer backbone C-F stretching vibrations, 25,33 the changes through the spectral region provide additional evidence for increasing ionomer aggregation and development of the hydrophobic, fluorocarbon-rich regions that are precursors to the ionomer film structural framework. It is important to note, however, the transformation of the aqueous dispersion to the aggregate-rich gel-phase is accompanied by refractive index variations that affect infrared beam propagation at the sample-ATR crystal interface and can cause distortion in strong absorption bands. 16,18 To demonstrate the impact of ATR sampling distortion, FTIR transmission spectra were recorded of the dilute dispersion and condensed film (Figure S4). Transmission infrared cells are designed to minimize light reflection and ensure vibrational band positions and line shapes represent sample characteristics with only nominal perturbations. 48-50 Figure S4 shows that the dilute dispersion and thin condensed film FTIR spectra of Nafion are similar, and in particular, the spectrum of the densified film lacks the strong shifts in the C-F stretching bands toward low frequencies that are evident in the ATR FTIR

spectra. The spectra in Figure S2 generated from electromagnetic field calculations provide further confirmation of the optical effects. The calculated spectra for the 20-µm and 50-µm films indicate the types of band distortions that can be expected to develop in performing ATR measurements on densified Nafion films having thicknesses greater than the evanescent wave penetration depth. These calculated spectra are in good agreement with the experimental ATR FTIR spectrum of the fully condensed film. Furthermore, having comparable features through the C-F stretching region in the dilute dispersion and thin condensed film transmission spectra is consistent with the insensitivity of mid-FTIR spectra to structural ordering in PTFE.<sup>34</sup> Although optical dispersion distortion makes it difficult to derive structural information from ionomer framework spectral features in the ATR FTIR spectra in Figure 1, the onset of the strong spectral variation through the C-F stretching region is useful as it signals gel-phase development and provides another marker

for the dispersion-to-gel phase transition region.

Features in the 32 h spectrum in Figure 1 are characteristic of the hydrated solid membrane phase. In typical experiments, exposing the sample to a flow of dry, N<sub>2</sub> gas did not perturb the strong framework bands in the 1200 cm<sup>-1</sup> - 1160 cm<sup>-1</sup> region appreciably, but produced an upshift in the 1058 cm<sup>-1</sup> band characteristic of -SO<sub>3</sub>-group dehydration (Figure S2).<sup>27,28,51</sup> It is worthwhile to mention that spectra



<u>Figure 4</u>. Data derived from confocal Raman microscopy measurements that followed Nafion thin film formation from an individual aqueous dispersion droplet. Dispersion properties are given in the legend to Figure 2. Black symbols, left y-axis: The inverse of  $I_{1058}$  plotted versus time. Blue symbols, right y-axis: Ionomer mass % derived from  $I_{1058}$  (see text for details). The dashed line is the least squares fit to the data covering the 0-3.8 h period ( $R^2 = 0.973$ ). The inset sketch depicts the confocal Raman microscopy sampling configuration.

identical to those in Figure 1 were recorded in measurements on H<sup>+</sup> exchanged ionomer dispersion. Upon drying the solid membrane ( $\geq 32$  h, Figure 1) under a flow of N<sub>2</sub> gas, H<sup>+</sup> exchanged samples displayed additional bands near 1412 cm<sup>-1</sup> and 910 cm<sup>-1</sup> signaling -SO<sub>3</sub>H formation. <sup>52,53</sup> 3.4. Confocal Raman microscopy measurements. The trends depicted in Figure 3 also are evident in the intensity variation of the hydration sensitive, sidechain end group vibration near 1058 cm<sup>-1</sup> derived from Raman spectra that monitor the drying of an individual Nafion dispersion droplet (Figures 4 and S5). Since Raman scattering intensities (I) scale directly with analyte concentration, <sup>54</sup> (I)<sup>-1</sup> is expected to have the same functional form as (pATR)<sup>-1</sup> defined in Eqns 1 and 2. The plot in Figure 4 tracking the Raman scattering in the peak at 1058 cm<sup>-1</sup> ( $I_{1058}$ ) initially decreases in accord with Eq 2 and, similar to the trend in Figure 3, begins to deviate from the initial linear response as the ionomer concentration in the droplet approaches the critical gelation point. Compared to Figure 3, however, the  $(I_{1058})^{-1}$  data points at early times have considerably greater scatter and the rate of decline in the vicinity of the critical gelation point appears to become faster rather than slower. The differences in variance in the data at early times reflects a limited ability to detect Raman signals from ionomer at dilute dispersion concentrations and complications from fluctuations in concentration gradients that develop within the evaporating droplet (vide infra). The infrared absorption measurements (Figures 1 and 3) achieve better detection limits for ionomer in the dilute dispersion. Nevertheless, the confocal Raman measurement has the potential for greater flexibility in the selection of vibrational bands for analysis, since Raman scattering at visible frequencies avoids the deleterious optical effects inherent in ATR FTIR sampling. For example, Figures S5 and S6 show the strong C-F stretching feature near 734 cm<sup>-1</sup> remains undistorted throughout the experiment and follows the time dependence of the 1058 cm<sup>-1</sup> band (Figure 4).

Near the dispersion-to-gel phase transition point, the different responses for the techniques can be traced in part to the effect of refractive index change within the sample on collection efficiency in the confocal microscopy measurement.<sup>55</sup> Transitioning from the dilute aqueous dispersion to the ionomer film achieves a closer match to the immersion fluid refractive index (n = 1.51 near 647 nm). Refractive index matching at frequencies of the Raman excitation and scattered photons reduces optical aberration and increases the radiation intensity within the confocal probe volume.<sup>55</sup> The resulting enhancement in spectral sensitivity is consistent with the steeper slope in the ( $I_{1058}$ )<sup>-1</sup> response as the dispersion passes through the 3.5 hour point in Figure 4. The slope change occurs just ahead of the dispersion critical gelation point and, as discussed further below, the rapid change in the water mass fraction.

A second factor that has potential to affect the Raman measurement is the small size of the confocal probe volume (~ 5 fL)<sup>19-21</sup> relative to the droplet. Since the droplet changes shape and can develop concentration gradients during drying,<sup>43,44,46</sup> Raman spectral features, particularly at early drying times, can be affected by inner fluid convective flow and chemical heterogeneity. In contrast, the cell design and volumes utilized in the ATR FTIR experiments ensured, like the gravimetric studies, that measurements near the gelation point reflect properties of the composite sample. Experiments are in progress to examine the sensitivity of confocal Raman microscopy to variations in drying behavior at different spatial positions within an ionomer dispersion droplet and the impacts of variable drying rates on ionomer film properties of importance to polymer electrolyte energy conversion devices.<sup>1</sup>

Also notable, close to the endpoint in the Raman experiment (Figure 4), the sample plateau at about 75 wt % is somewhat lower than expected based on the response recorded in the gravimetric measurement (~85 wt %). The difference is traceable to the estimation of sample density (Section

2.5) and breakdown in the ideal solution approximation as condensed film properties become dominant. Beyond the gelation point, the mass % scale in Figure 4 underestimates the sample composition.

3.5. Tracking water as a probe of gelation. Since the water spectral band intensities are directly proportional to the water molar concentration in the dispersion,<sup>54</sup> they provide another possible means to track progress toward ionomer gelation. To test the sensitivity of this approach, the behavior of the relatively narrow band for the water H-O-H bending vibration near 1645 cm<sup>-1</sup> was scrutinized. The plots in Figure 5 were derived from the full ATR IR and Raman spectral data sets

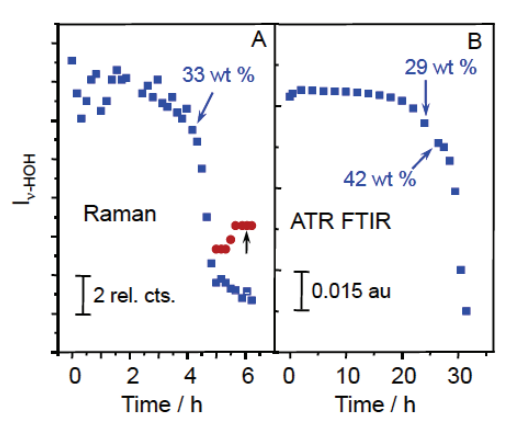


Figure 5. Water H-O-H bending vibrational band intensities (blue squares) from (A) confocal Raman microscopy and (B) ATR FTIR spectra. See Figures 3 and 4 for details. The arrows indicate the ionomer 33 wt % point.

reported (Figures 1 and S5, respectively). With water well in excess initially, the water concentration change is slow at early evaporation times. However, Figure 5 shows the water spectral signal drops rapidly at the dispersion critical gelation point. The gravimetric data from Figure 2, when expressed in terms of water concentration (Figure 6A), follows the same trend. The responses in Figure 5 and 6A can be understood from a simple simulation of the gravimetric

experiment (Figure 6B). Figure 6B tracks the water concentration in an initially 5 wt % ionomer dispersion as water evaporation occurs at a constant rate of 0.33 mg/min, close to the rate observed in Figure 2. The simulated results show a sharp decline in the water mass fraction is expected when the ionomer reaches approximately 1/3 of the total dispersion mass, or when Eq 1  $\approx$  33 wt %. This ionomer fraction is within the range of the critical gelation point for the aqueous dispersion (34  $\pm$  4 wt %). Thus, the roughly constant water evaporation rate from the dispersion observed in the

ATR FTIR, Raman and gravimetric experiments considered leads to the rapid change in water concentration, and hence measured signal, near the critical gelation concentration. In Figure 5A,

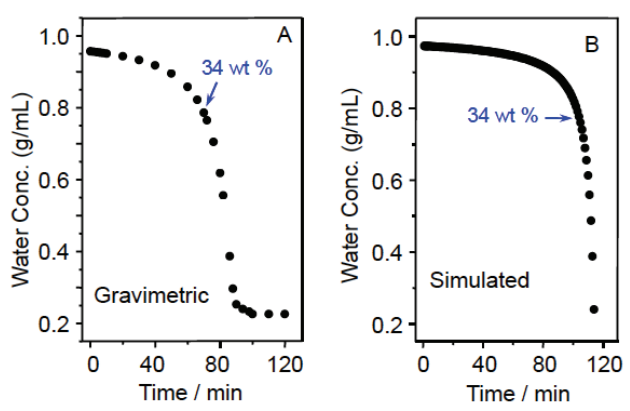


Figure 6. (A) Plot of water concentration as a function of time derived from the Nafion ionomer dispersion data in Figure 2. The points closest to the gelation transition (~34 wt %) are indicated in each plot. In A, the red circles and upward black arrow indicate the transition near 5.5 min in the hydration sensitive 1058 cm<sup>-1</sup> feature to 1067 cm<sup>-1</sup>. (B) Simulated plot of water concentration versus time for a constant rate of water loss from an aqueous ionomer dispersion sample initially at 5 wt %. The arrows indicate the ionomer 33 wt % point.

the included filled circular symbols indicate the point of upshift in the hydration sensitive 1058 cm<sup>-1</sup> feature to 1067 cm<sup>-1</sup>. The upshift is characteristic of the strengthened metal cation / sulfonate group interactions that accompany sulfonate group dehydration.<sup>27,56</sup> The transition occurs well beyond the critical gelation point and indicates the sulfonate groups remain fully solvated through gel-phase, the as anticipated.

### 4. Conclusions

In the study of aqueous Nafion ionomer dispersions, ATR FTIR spectroscopy and confocal Raman microscopy are sensitive to the vibrational modes of ionomer particles and report progress during the transformation to gel and solid membrane phases. The well-resolved peak near 1058 cm<sup>-1</sup> associated with coupled motions of the Nafion sidechain C-O-C and -SO<sub>3</sub>- groups<sup>32,33,35</sup> is a sensitive probe of gel-phase development. In ATR FTIR measurements, the persistence of hydration water in the vicinity of the sidechain end groups helps maintain a constant local solvation environment that limits optical distortion in the 1058 cm<sup>-1</sup> peak as the ionomer assembles into the phase-separated framework structure of the solid membrane. Confocal Raman microscopy offers

a unique advantage in enabling spatial probing within a drying dispersion droplet, and thus, the potential to detect ionomer concentration gradients<sup>43,44,46</sup> that can impact homogeneity of thin ionomer films vital to the operation of polymer electrolyte fuel cell and electrolyzer devices and chemical sensing platforms. Both vibrational spectroscopy techniques predict trends in evaporative water loss and entry into the gel-phase consistent with expectations of gravimetric measurements and earlier studies<sup>3,12</sup> of Nafion ionomer dispersion properties. Dependent upon the solvent, critical gelation concentrations for Nafion ionomer dispersions have been reported to vary from 4 wt% to 56 wt% (2 vol% to 40 vol%) and to correlate with the tensile toughness of cast films.<sup>3</sup> The reported findings demonstrate new approaches to investigate these solvent effects and motivate more quantitative studies that include control of sample temperature and surrounding gas-phase composition.

## Acknowledgments

We thank Dr. Yu Seung Kim (Los Alamos National Laboratory) for insightful discussions concerning ionomer dispersion properties and advice on the ion-exchange procedures used. We are grateful for support from the Office of Science, U.S. Department of Energy, through grant DE-FG03-93ER14333 and the U.S. National Science Foundation through grant CBET-1922956 and CBET-1921075. CK also is thankful for support from the Texas Tech University faculty development leave program.

#### References

- 1. Karan, K. Interesting facets of surface, interfacial, and bulk characteristics of perfluorinated ionomer films *Langmuir* **2019**, *35*, 13489–13520.
- 2. Kusoglu, A.; Weber, A. Z. New insights into perfluorinated sulfonic-acid ionomers *Chem. Rev.* **2017**, *117*, 987-1104.

- 3. Kim, Y. S.; Welch, C. F.; Hjelm, R. P.; Mack, N. H.; Labouriau, A.; Orler, E. B. Origin of toughness in dispersion-cast Nafion membranes *Macromolecules* **2015**, *48*, 2161-2172.
- 4. Sharif, I.; Creager, S. E.; DesMarteau, D. D., Fluorinated ionomers and ionomer membranes containing the bis[(perfluoroalkyl)sulfonyl] imide protogenic group In Handbook of Fluoropolymer Science and Technology; Smith, D. W., Jr., Iacono, S. T. and Iyer, S. S., Ed.; Wiley, 2014, pp 523-545.
- 5. Mauritz, K. A.; Moore, R. B. State of understanding Nafion *Chem. Rev.* **2004**, *104*, 4535-4585.
- 6. Xiao, T.; Wu, F.; Hao, J.; Zhang, M.; Yu, P.; Mao, L. In vivo analysis with electrochemical sensors and biosensors *Anal. Chem.* **2017**, *89*, 300-313.
- 7. Paul, D. K.; Karan, K.; Docoslis, A.; Giorgi, J. B.; Pearce, J. Characteristics of self-assembled ultrathin Nafion films *Macromolecules* **2013**, *46*, 3461-3475.
- 8. Hamrock, S. J.; Yandrasits, M. A. Proton exchange membranes for fuel cell applications *J. Macromolecular Sci., Part C: Polymer Reviews* **2006**, *46*, 219-244.
- 9. Korzeniewski, C.; Liang, Y.; Zhang, P.; Sharif, I.; Kitt, J. P.; Harris, J. M.; Hamrock, S. J.; Creager, S. E.; DesMarteau, D. D. Vibrational spectroscopy for the determination of ionizable group content in ionomer materials *Appl. Spectrosc.* **2018**, *72*, 141-150.
- 10. Moore, R. B., III; Martin, C. R. Procedure for preparing solution-cast perfluorosulfonate ionomer films and membranes *Anal. Chem.* **1986**, *58*, 2569-2570.
- 11. Moore, R. B., III; Martin, C. R. Chemical and morphological properties of solution-cast perfluorosulfonate ionomers *Macromolecules* **1988**, *21*, 1334-1339.
- 12. Welch, C.; Labouriau, A.; Hjelm, R.; Orler, B.; Johnston, C.; Kim, Y. S. Nafion in dilute solvent systems: Dispersion or solution? *ACS Macro. Lett.* **2012**, *1*, 1403-1407.
- 13. Kollath, V. O.; Liang, Y.; Mayer, F. D.; Ma, X.; Korzeniewski, C.; Karan, K. Model-based analyses of confined polymer electrolyte nanothin films experimentally probed by polarized ATR-FTIR spectroscopy *J. Phys. Chem. C* **2018**, *122*, 9578–9585.
- 14. Bukola, S.; Liang, Y.; Korzeniewski, C.; Harris, J.; Creager, S. E. Selective proton/deuteron transport through Nafion|graphene|Nafion sandwich structures at high current density *J. Am. Chem. Soc.* **2018**, *140*, 1743-1752.

- 15. Bertie, J. E.; Eysel, H. H. Infrared intensities of liquids I: Determination of infrared optical and dielectric constants by FT-IR using the CIRCLE ATR cell *Appl. Spectrosc.* **1985**, *39*, 392-400.
- 16. Woods, D. A.; Bain, C. D. Total internal reflection spectroscopy for studying soft matter *Soft Matter* **2014**, *10*, 1071-1096.
- 17. Griffiths, P. R.; de Haseth, J. A. *Fourier Transform Infrared Spectrometry*; 2nd ed.; Wiley: Hoboken, NJ, 2007.
- 18. Porter, M. D. IR External Reflection Spectroscopy: A Probe for Chemically Modified Surfaces *Anal. Chem.* **1988**, *60*, 1143A-1155A.
- 19. Kitt, J. P.; Bryce, D. A.; Harris, J. M. Spatial filtering of a diode laser beam for confocal Raman microscopy *Appl. Spectrosc.* **2015**, *69*, 513-517.
- 20. Bridges, T.; Houlne, M.; Harris, J. M. Spatially resolved analysis of small particles by confocal Raman microscopy: Depth profiling and optical trapping *Anal. Chem.* **2004**, *76*, 576-584.
- 21. Korzeniewski, C.; Kitt, J. P.; Bukola, S.; Creager, S. E.; Minteer, S. D.; Harris, J. M. Single layer graphene for estimation of axial spatial resolution in confocal Raman microscopy depth profiling *Anal. Chem.* **2019**, *91*, 1049-1055.
- 22. Oberbroeckling, K. J.; Dunwoody, D. C.; Minteer, S. D.; Leddy, J. Density of Nafion exchanged with transition metal complexes and tetramethyl ammonium, ferrous, and hydrogen ions: Commercial and recast films *Anal. Chem.* **2002**, *74*, 4794-4799.
- 23. Quezado, S.; Kwak, J. C. T.; Falk, M. An infrared study of water-ion interactions in perfluorosulfonate (Nafion) membranes *Can. J. Chem.* **1984**, *62*, 958-966.
- 24. Blanchard, R. M.; Nuzzo, R. G. An infrared study of the effects of hydration on cation-loaded Nafion thin films *J. Polym. Sci.: Part B: Polym. Phys.* **2000**, *38*, 1512-1520.
- 25. Gruger, A.; Regis, A.; Schmatko, T.; Colomban, P. Nanostructure of Nafion membranes at different states of hydration An IR and Raman study *Vib. Spectrosc.* **2001**, *26*, 215-225.
- 26. Buzzoni, R.; Bordiga, S.; Ricchiardi, G.; Spoto, G.; Zecchina, A. Interaction of H<sub>2</sub>O, CH<sub>3</sub>OH, (CH<sub>3</sub>)<sub>2</sub>O, CH<sub>3</sub>CN, and pyridine with the superacid perfluorosulfonic membrane Nafion: An IR and Raman study *J. Phys. Chem.* **1995**, *99*, 11937-11951.

- 27. Korzeniewski, C.; Adams, E.; Liu, D. Responses of hydrophobic and hydrophilic groups in Nafion differentiated by least squares modeling of infrared spectra recorded during thin film hydration *Appl. Spectrosc.* **2008**, *62*, 634-639.
- 28. Kunimatsu, K.; Bae, B.; Miyatake, K.; Uchida, H.; Watanabe, M. ATR-FTIR study of water in Nafion membrane combined with proton conductivity measurements during hydration/dehydration cycle *J. Phys. Chem. B* **2011**, *115*, 4315–4321.
- 29. Eisenberg, A.; Yeager, H. L. *Perfluorinate Ionomer Membranes*; Eisenberg, A.; Yeager, H. L., Ed.; American Chemical Society: Washington DC, 1982.
- 30. Cable, K. M.; Mauritz, K. A.; Moore, R. B. Effects of hydrophilic and hydrophobic counterions on the coulombic interactions in perfluorosulfonate ionomers *J. Polym. Sci.: Part B: Polym. Phys.* **1995**, *33*, 1065-1072.
- 31. Webber, M.; Dimakis, N.; Kumari, D.; Fuccillo, M.; Smotkin, E. S. Mechanically coupled internal coordinates of ionomer vibrational modes *Macromolecules* **2010**, *43*, 5500-5502.
- 32. Warren, D. S.; McQuillan, A. J. Infrared spectroscopic and DFT vibrational mode study of perfluoro(2-ethoxyethane) sulfonic acid (PES), a model Nafion side-chain molecule *J. Phys. Chem. B* **2008**, *112*, 10535-10543.
- 33. Kendrick, I.; Kumari, D.; Yakaboski, A.; Dimakis, N.; Smotkin, E. S. Elucidating the ionomer-electrified metal interface *J. Am. Chem. Soc.* **2010**, *132*, 17611-17616.
- 34. Starkweather, H. W. J.; Ferguson, R. C.; Chase, D. B.; Minor, J. M. Infrared spectra of amorphous and crystalline poly(tetrafluorethylene) *Macromolecules* **1985**, *18*, 1684-1686.
- 35. Danilczuk, M.; Lin, L.; Schlick, S.; Hamrock, S. J.; Schaberg, M. S. Understanding the fingerprint region in the infra-red spectra of perfluorinated ionomer membranes and corresponding model compounds: Experiments and theoretical calculations *J. Power Sources* **2011**, *196*, 8216-8224.
- 36. Negro, E.; Vittadello, M.; Vezzu, K.; Paddison, S. J.; Di Noto, V. The influence of the cationic form and degree of hydration on the structure of Nafion *Solid State Ionics* **2013**, *252*, 84-92.
- 37. Hallinan, D. T.; De Angelis, M. G.; Baschetti, M. G.; Sarti, G. C.; Elabd, Y. A. Non-Fickian diffusion of water in Nafion *Macromolecules* **2010**, *43*, 4667-4678.

- 38. Giffin, G. A.; Haugen, G. M.; Hamrock, S. J.; Di Noto, V. Interplay between structure and relaxations in perfluorosulfonic acid proton conducting membranes *J. Am. Chem. Soc.* **2013**, *135*, 822-834.
- 39. Wong, J. S.; Rein, A. J.; Wilks, D.; Wilks, P., Jr. Infrared spectroscopy of aqueous antibiotic solutions *Appl. Spectrosc.* **1986**, *38*, 32-35.
- 40. Birdi, K. S.; Vu, D. T. A study of evaporation rates of small water drops placed on a solid surface *J. Phys. Chem.* **1989**, *93*, 3702-3703.
- 41. Ozturk, T.; Erbil, H. Y. Evaporation of water-ethanol binary sessile drop on fluoropolymer surfaces: Influence of relative humidity *Colloids Surf. A* **2018**, *553*, 327-336.
- 42. Erbil, H. Y. Evaporation of pure liquid sessile and spherical suspended drops: A review *Adv. Colloid Interface Sci.* **2012**, *170*, 67-86.
- 43. Shi, J.; Yang, L.; Bain, C. D. Drying of ethanol/water droplets containing silica nanoparticles *ACS Appl. Mater. Interfaces* **2019**, *11*, 14275-14285.
- 44. Anyfantakis, M.; Baigl, D.; Binks, B. P. Evaporation of drops containing silica nanoparticles of varying hydrophobicities: Exploiting particle-particle interactions for additive-free tunable deposit morphology *Langmuir* **2017**, *33*, 5025-5036.
- 45. Talbot, E. L.; Yang, L.; Berson, A.; Bain, C. D. Control of the particle distribution in inkjet printing through an evaporation-driven sol-gel transition *ACS Appl. Mater. Interfaces* **2014**, *6*, 9572-9583.
- 46. Brutin, D.; Starov, V. Recent advances in droplet wetting and evaporation *Chem. Soc. Rev.* **2018**, *47*, 558-585.
- 47. Kreuer, K.-D. Ion conducting membranes for fuel cells and other electrochemical devices *Chem. Mater.* **2014**, *26*, 361-380.
- 48. Young, R. P.; Jones, R. N. The shapes of infrared absorption bands of liquids *Chem. Rev.* **1971**, *71*, 219-228.
- 49. Hawranek, J. P.; Jones, R. N. The control of errors in i.r. spectrophotometry -- V. Assessment of errors in the evaluation of optical constants by transmission measurements on thin films *Spectrochim. Acta* **1976**, *32A*, 99-109.
- 50. Hawranek, J. P.; Neelakantan, P.; Young, R. P.; Jones, R. N. The control of errors in i.r. spectrophotometry -- III. Transmission measurements using thin cells *Spectrochim. Acta* **1976**, *32A*, 75-84.

- 51. Iwamoto, R.; Oguro, K.; Sato, M.; Iseki, Y. Water in perfluorinated sulfonic acid nafion membranes *J. Phys. Chem. B* **2002**, *106*, 6973-6979.
- 52. Kendrick, I.; Yakaboski, A.; Kingston, E.; Doan, J.; Dimakis, N.; Smotkin, E. S. Theoretical and experimental infrared spectra of hydrated and dehydrated Nafion *J. Polym. Sci. Part B: Polym. Phys.* **2013**, *51*, 1329-1334.
- 53. Basnayake, R.; Peterson, G. R.; Casadonte, D. J., Jr.; Korzeniewski, C. Hydration and interfacial water in Nafion membrane probed by transmission infrared spectroscopy *J. Phys. Chem. B* **2006**, *110*, 23938-23943.
- 54. McCreery, R. L. *Raman Spectroscopy for Chemical Analysis*; Wiley: New York, 2000; Vol. 157.
- 55. Hell, S.; Reiner, G.; Cremer, C.; Stelzer, E. H. K. Aberrations in confocal fluorescence microscopy induced by mismatches in refractive index *J. Microscopy* **1993**, *169*, 391-405.
- 56. Lowry, S. R.; Mauritz, K. A. An investigation of ionic hydration effects in perfluorosulfonate ionomers by Fourier transform infrared spectroscopy *J. Am. Chem. Soc.* **1980**, *102*, 4665-4667.